Asymmetric Arp2/3-mediated actin assembly facilitates clathrin-mediated endocytosis at stalled sites in genome-edited human stem cells

Meiyan Jin[1*], Cyna Shirazinejad[1, 2*], Bowen Wang[3], Amy Yan[1], Johannes Schöneberg[1, 4], Srigokul Upadhyayula[1], Ke Xu[3], David G. Drubin[1#]

[1] Department of Molecular and Cell Biology, University of California, Berkeley, CA 94720

[2] Biophysics Graduate Group, University of California Berkeley; Berkeley, CA, 94720

[3] Department of Chemistry, University of California, Berkeley, CA 94720

[4] Current address: Department of Pharmacology, and Department of Chemistry and Biochemistry, University of California, San Diego, CA 92093

[*]These authors contributed equally.

[#]Correspondence to DGD (drubin@berkeley.edu)

Author contributions

MJ, CS and DGD conceived the study and experiments. MJ and AY generated the genome-edited cell lines. MJ performed live cell data acquisition and sample preparation for super-resolution microscopy. BW and KX performed super-resolution microscopy and super-resolution data reconstruction. CS developed computational analysis tools and SU, JS, and MJ supported the data analysis. MJ and CS prepared the figures and MJ and DGD wrote the manuscript with feedback from the other authors.

Abstract

Actin filament assembly facilitates vesicle formation in several trafficking pathways including clathrin-mediated endocytosis (CME)[1,2]. However, how actin assembly forces are harnessed has not been fully revealed for any vesicle forming process. In this study, three-dimensional (3D) super-resolution microscopy, live-cell imaging of triple-genome-edited, induced pluripotent stem cells (iPSCs), and newly developed machine-learning-based computational analysis tools, were used to comprehensively analyze assembly dynamics and geometry of proteins representing three different CME functional modules. When hundreds of CME events with and without associated Arp2/3-dependent actin network assembly were compared, sites with actin assembly showed a distinct delay between completion of endocytic coat expansion and vesicle scission, consistent with the notion that these were stalled sites requiring actin assembly forces to complete vesicle formation. Importantly, our analysis showed that N-WASP is preferentially recruited to one side of CME sites, where it stimulates actin assembly asymmetrically. These results indicate that in mammalian cells actin assembly is induced at stalled CME sites, where asymmetric forces pull the plasma membrane into the cell much like a bottle opener pulls off a bottle cap.

Main

Formation of clathrin-coated vesicles requires forces to first bend the membrane into a sphere or tube, and to then break the thin neck that connects the vesicle to the plasma membrane. These forces are generated through the combined actions of proteins that directly bend the membrane and actin filament assembly[3–5] (Fig. 1a). A detailed understanding of how actin forces are harnessed to aid vesicle formation and scission, and whether and how actin assembly

might mediate an adaptive response to the opposing forces such as membrane tension and turgor pressure, depends on understanding where filament assembly occurs around the endocytic membrane and when. In yeast cells, where turgor pressure is particularly high, super-resolution data suggest that actin assembles symmetrically around CME sites and indicate that actin regulators including Las17, yeast WASP, is present in a ring surrounding the base of the clathrin coat[6]. However, studies on mammalian cells raised the possibility that actin assembly may at least in some cases be initiated asymmetrically at clathrin coats[7–9]. Which CME sites assemble actin, and how actin networks are organized with respect to CME sites, has not been determined systematically, in a large-scale, unbiased manner, particularly in live mammalian cells. This information is essential to understanding how and why actin assembly forces are harnessed for CME.

To investigate the physiological roles and spatiotemporal regulation of actin assembly at CME sites in mammalian cells, we applied genome-editing techniques to generate a human iPSC line (hereafter referred to as ADA cells) that co-expresses a TagRFP-T fusion of the mu1 subunit of the AP2 adaptor complex (AP2M1), a TagGFP2 fusion of dynamin2 (DNM2), and a HaloTag fusion of the ARPC3 subunit of the Arp2/3 complex as representatives of the CME coat, scission and actin modules respectively[3,10,11] (Fig. 1a, Extended Data Fig. 1a, b and Supplementary Video 1, 2). Previous studies showed that endogenously tagged AP2M1, DNM2 and ARPC3 can serve as reliable markers of these CME functional modules that avoid disruption of physiological spatiotemporal organization of the process as might be caused by overexpression of fluorescently labeled proteins[12–15]. We observed dynamic CME events on the basal plasma membrane of the genome-edited cells using Total Internal Reflection Fluorescence (TIRF) microscopy (Extended Data Fig. 1b). Consistent with previous studies, AP2 is recruited

at early CME stages while DNM2 is recruited in two phases[10,15–17]. At the early stage of CME, a relatively small amount of DNM2 is recruited to CME sites. Shortly before the end of a CME event, the DNM2 recruitment rate increases rapidly with DNM2 levels reaching a peak concomitant with vesicle scission[10,15,18] (Extended Data Fig. 1b). This later rapid-recruitment phase represents the assembly of dynamin helix on the highly curved neck of the budding vesicle after the U to Ω shape transition of the endocytic membrane[15,18–21].

We analyzed how actin networks are organized at CME sites in both fixed and live cells. First, we performed two-color 3D Stochastic Optical Reconstruction Microscopy (STORM) imaging[22] on fixed ADA cells, localizing either AF647 phalloidin-labeled actin filaments[23] or HaloTag-fused ARPC3 at CME sites. Due to the dense phalloidin labelling of cortical actin filaments under plasma membrane, it was often challenging to unambiguously identify the CME-specific actin structures in iPSCs. However, in regions with thinner cortical actin layers, we observed that actin was typically distributed asymmetrically around CME sites (Fig. 1b and Extended Data Fig. 2a). Antibody labeling of ARPC3-Halotag in the ADA cells had the advantage of a less complex staining pattern. Besides being highly concentrated in lamellipodia, ARPC3 was associated with CME sites asymmetrically, like actin (Fig 1c and Extended Data Fig. 2b). These data indicate that ARPC3 can be used to study Arp2/3-mediated actin assembly at CME sites as a more specific maker of branched actin networks than a general actin label.

We next used ADA cells to investigate actin assembly at CME sites in live cells, which has several advantages over studies in fixed cells. During the fixation and subsequent sample preparation, actin structures may not be faithfully preserved. In addition, in fixed cells it is very difficult to identify the stage of the CME, so the timing, geometry and dynamics of actin assembly cannot be related to the endocytic stage. More importantly, only by using live cells is it

possible to trace a single CME event from start to finish, and to therefore identify those CME events wherein no detectable actin is ever assembled to compare key parameters between events with and without associated actin assembly.

By visualizing endogenously tagged AP2M1 to mark the initiation of CME, and DNM2 to mark scission, together with ARPC3 to specifically label Arp2/3-nucleated, branched actin filaments (Fig. 1a), we were able to precisely study the spatial and temporal regulation of actin assembly during CME. Using TIRF live-cell imaging, we observed ARPC3-labeled branched actin networks at lamellipodia and a subpopulation of CME sites (Fig. 2a, b). Dynamic actin assembly and disassembly occurred at CME sites with different spatio-temporal characteristics, including discrete CME sites, clathrin plaques and at clathrin coat splitting sites, as previously reported[7] (Fig. 2c and Extended Data Fig. 3a, b). In the analysis described below, we focus on the discrete CME events and not the more complex ones (plaques and splitting events). Quantitative analysis of these events with 1s/frame temporal resolution revealed that ARPC3 is mainly recruited during the late stages of CME with similar timing to the rapid recruitment stage of DNM2[14] (Fig. 2b, c). Interestingly, we observed clear spatial displacement between ARPC3 (actin module) and AP2 (coat module) before and after vesicle scission (Fig. 2c). Imaging fluorescent beads using the same settings indicates that the displacement is not an artifact caused by misalignment between different imaging channels (Supplementary Video 3 and Extended Data Fig. 3c).

To analyze the intrinsic recruitment order and timing for up to three endocytic proteins at CME sites quantitatively and systematically, we developed a high-throughput method that does not involve any manual selection of CME sites, which is prone to bias (see Materials and Methods). Briefly, AP2 tracks were identified using standard particle-tracking algorithms[24].

Novel filtering methods then extracted DNM2-positive events marked by one or more DNM2 burst. The AP2 and DNM2 tracks were decomposed into dynamic features describing the events' position and brightness. These features were used for clustering via unsupervised machine learning, which enabled grouping of similarly-behaved tracks (Extended Data Fig. 4a and b). DNM2-positive events were refined by a detection scheme that determined the number of DNM2 peaks using various characteristics of a single DNM2-peak: the peak height, width, and minimum peak-to-peak distance (Extended Data Fig. 4c). Events with a single DNM2 peak were analyzed as described below. The method detects low signals from endogenously tagged CME proteins, such as the low-level recruitment of DNM2 at the early stages of CME, and accurately reveals the different CME stages (Extended Data Fig. 4d).

Next, the timing of actin network assembly at CME sites was determined using ARPC3 as a branched actin filaments marker by analyzing over one thousand CME events. Although actin appearance early in CME has been reported[7], determining the actin assembly timing is challenging because actin dyes lack the specificity required to distinguish newly assembled branched actin at CME sites from the nearby cortical actin filaments or actin filaments attached to other vesicles or organelles. Also, whether actin functions during the early stage of CME has not yet been shown conclusively due to the potential side effects such as changes in membrane tension caused by actin inhibitors. Our endogenous ARPC3 tagging approach sidesteps these problems. We classified ARPC3 positive CME events into two groups: one with ARPC3 appearance early in CME and the other late in CME (Fig. 3a). We observed that in most of the events (N=1,385, 67.8%) a sharply increasing ARPC3 signal appears with similar timing to the rapid-recruitment phase of DNM2 concomitant with the U to Ω membrane shape transition. This timing is consistent with previously proposed role for actin in membrane invagination, as studies

showed that actin inhibitors block the U to Ω endocytic membrane shape transition[25]. In some cases (N=657, 32.2%) we detected ARPC3 signals at early CME stages. To test whether random overlap between nearby actin structures and CME sites might be responsible for the apparent early actin recruitment, we generated a randomized data set by pairing ARPC3 images with AP2 and DNM2 images from an unrelated movie (Fig. 3b). In this data set, we detected early "assembly" of actin in the majority of ARPC3 positive CME events (N=17,282, 72.9%), and the intensity profiles of these events resembled the early-actin CME events we observed in the real data set (Fig. 3a, b). Therefore, we conclude that the presence of actin early in CME is very likely due to unrelated nearby actin structures overlapping with CME sites.

Our live-cell analysis allowed the timing of branched actin network assembly to be compared to the scission timing, and the spatial offset between the clathrin coat and the associated actin network to be determined. Super-resolution imaging of yeast CME sites suggested that actin and actin nucleators localize symmetrically in a ring around CME sites, and computational modeling suggested that an asymmetric actin arrangement would not provide sufficient force for the membrane invagination during yeast CME[6]. In contrast, in mammalian cells, which require less actin force production during CME, imaging of fixed cells suggested that actin structures associate adjacent to apparent flat clathrin coats. However, these studies proposed that at the later CME stages the actin structures become larger and more symmetric to provide sufficient force for membrane deformation and scission[7,8]. Surprisingly, in our live cell studies designed to highlight sites of new actin assembly, we observed off-centered branched actin networks at CME sites throughout even the latest CME stages (Fig. 2c). Furthermore, most ARPC3-positive CME sites accomplish scission within 30s from the initiation of ARPC3 recruitment (Fig. 3c). The actin networks were off center from the coat signals by approximately

150nm at the time of vesicle scission (Fig. 3d). This observation is consistent with the observation that ring-shaped actin structures at clathrin coats were rarely observed in the high-resolution, live-cell imaging in a previous study[26]. In total, these live-cell data suggest that in mammalian cells, asymmetric actin network assembly can provide enough force to assist membrane deformation and scission during the late stages of CME.

To gain new insights into the function of this asymmetric actin network assembly, we quantitatively compared CME events with or without ARPC3 recruitment. We observed that about 30% of CME events are completed in the absence of detectable actin assembly, which is consistent with the hypothesis that in mammalian cells actin assembly is required for CME only under relatively high membrane tension, which can vary regionally within cells[9,25]. Consistent with the possibility that increased membrane tension stalls membrane deformation during CME[5,27,28], CME lifetimes were markedly longer for ARPC3 positive events compared to the ARPC3 negative events (Fig. 4a). In addition, when the AP2M1 intensity vs time profiles were compared between ARPC3 positive and negative CME sites, a plateau, which lasts for approximately 10 seconds, was observed for the ARPC3 positive events (Fig. 4b). Based on these observations and previous experimental and computational modeling data[5,9,25], we propose that this plateau in branched actin-positive CME events represents stalled membrane bending due to an unfavorable local membrane environment, such as higher membrane tension[5,27,28].

We hypothesized that the asymmetric actin network might affect the lateral movements of endocytic coats on the plasma membrane. Interestingly, the ARPC3 positive CME sites showed significantly slower, but more directional lateral movement before the scission compared to the ARPC3 negative CME sites (Fig. 4c, d). After scission both ARPC3 positive and negative vesicles showed fast, apparently random movements (Fig. 4c, d). These data suggest that the

asymmetric actin can stabilize the forming endocytic coat while pushing it in the plane of the plasma membrane with a lateral directional force.

To further explore how the asymmetrical assembly of actin networks at CME sites is regulated, we endogenously tagged N-WASP, an actin nucleation promoting factor (NPF) that plays roles in CME, in AP2M1-tagRFP-T/ DNM2-tagGFP2 genome-edited iPSCs (hereafter referred to as ADW cells, Fig. 5a and Extended Data Fig. 5a). In these cells, N-WASP was recruited asymmetrically to CME sites at the late stage (Fig. 5b-d and Extended Data Fig. 5b, c). Longer lifetimes and a plateau in the AP2 intensity vs time plot were observed specifically in the N-WASP positive CME events (Extended Data Fig. 5d, e). These data indicate that asymmetric NPF recruitment underlies the asymmetric architecture of branched actin networks at CME sites.

Using large-scale, comprehensive analysis of thousands of CME sites, our study demonstrates that in mammalian cells coat assembly dynamics predict which sites will assemble actin, and show that at apparently stalled sites, actin assembles asymmetrically to facilitate successful vesicle formation.

Based on the data presented here, we propose an updated model of actin assembly at mammalian CME sites (Fig. 5e): (1) Where the local membrane tension is lower, (Fig. 5e upper scenario) the membrane can undergo flat-U-Ω shape transitions without actin assembly in a relatively short time. When the coat grows large enough to form a Ω-shaped bud, sufficient dynamin can be recruited to perform scission, and there is little delay between coat expansion and scission; (2) Where the local membrane tension is high and the coat protein-membrane interaction does not generate sufficient force to curve the membrane, extra force generation from actin assembly is required[5,25]. Asymmetric N-WASP recruitment activates actin nucleation mostly at one side of the clathrin coat, generating an asymmetric force that pulls the membrane

into the cell with a similar action to a bottle cap opener. We speculate that this asymmetrical force generates asymmetric membrane deformation at endocytic sites observed by high-speed atomic force microscopy[29] and may twist the clathrin pit to promote scission at the neck. CME events with associated actin assembly have longer lifetimes, likely due to a delay between coat expansion and scission, requiring adaptive recruitment of actin regulators followed by actin network assembly and membrane remodeling.

Under the cell culture conditions used in this study, we observed asymmetric actin assembly at CME sites in living mammalian cells, which is different from the symmetric actin structures observed at CME sites in yeasts[6], which grow under high turgor pressure and require actin assembly for membrane invagination[30]. However, interestingly, a recent study has shown that when the membrane tension is increased artificially, actin coverage over the clathrin coat is increased at CME sites in mammalian cells as well[9]. This observation, together with our new data, suggests that actin assembly at CME sites undergoes conserved but highly adaptive regulation in yeasts and mammalian cells. Asymmetric actin assembly is the default mode when a relatively small amount of force is sufficient to drive membrane remodeling. However, adaptive mechanisms result in assembly of larger or more symmetric actin structures that provide larger amounts of force to counter high membrane tension or turgor pressure.

Future computational modeling studies of how asymmetric actin network assembly provides forces for vesicle formation and membrane remodeling will deepen our understanding of actin's functions in a host of actin-mediated processes.

Our model provides further insights into the basis for inconsistent effects of actin drugs on CME[7,12,25,30–35]. Actin plays crucial roles in membrane shaping, cell adhesion, and membrane

tension. Global disruption of actin dynamics is expected to dramatically change membrane tension and therefore to have both direct and indirect effects on CME.

The results presented here also provide considerations relevant to the constant coat area vs constant coat curvature models for how the clathrin coat assembles and develops curvature. In the constant area model, flat clathrin coats grow close to their final size before becoming curved into a vesicle. In the constant curvature model, clathrin coats grow with a fixed curvature. These two models of CME are under active debate[27,36–39]. Our observations suggest that coat expansion and curvature generation may be regulated via distinct mechanisms, with different actin requirements. Our data show that at actin-positive CME sites, actin assembles at the late stage of CME when coat assembly is mostly completed (Fig. 3d and Extended Data Fig. 6a). In the constant curvature model, we would find actin-associated clathrin coats in only highly curved dome and spherical shapes (Extended Data Fig. 6b). However, actin-associated flat or shallow clathrin coats have been observed in multiple studies[8,9], which supports the constant area model at actin-positive CME sites (Extended Data Fig. 6c). Mathematical modeling predicts that at actin-negative CME sites, where coat proteins provide sufficient force to bend the membrane[23], the membrane smoothly evolves from a flat to budded morphology as the coat area increases[5], which supports constant curvature model. Therefore, in the future studies, the constant coat area and constant coat curvature models need to be tested separately on a single type of CME event.

REFERENCES

1. Rottner, K., Faix, J., Bogdan, S., Linder, S. & Kerkhoff, E. Actin assembly mechanisms at a glance. *J. Cell Sci.* **130**, 3427–3435 (2017).
2. Lanzetti, L. Actin in membrane trafficking. *Current Opinion in Cell Biology* (2007). doi:10.1016/j.ceb.2007.04.017
3. Lu, R., Drubin, D. G. & Sun, Y. Clathrin-mediated endocytosis in budding yeast at a glance. *J. Cell Sci.* **129**, 1531–6 (2016).
4. Lacy, M. M., Ma, R., Ravindra, N. G. & Berro, J. Molecular mechanisms of force production in clathrin-mediated endocytosis. *FEBS Letters* (2018). doi:10.1002/1873-3468.13192
5. Hassinger, J. E., Oster, G., Drubin, D. G. & Rangamani, P. Design principles for robust vesiculation in clathrin-mediated endocytosis. *Proc. Natl. Acad. Sci. U. S. A.* (2017). doi:10.1073/pnas.1617705114
6. Mund, M. *et al.* Systematic Nanoscale Analysis of Endocytosis Links Efficient Vesicle Formation to Patterned Actin Nucleation. *Cell* (2018). doi:10.1016/j.cell.2018.06.032
7. Yarar, D., Waterman-Storer, C. M. & Schmid, S. L. A dynamic actin cytoskeleton functions at multiple stages of clathrin-mediated endocytosis. *Mol. Biol. Cell* **16**, 964–975 (2005).
8. Collins, A., Warrington, A., Taylor, K. A. & Svitkina, T. Structural organization of the actin cytoskeleton at sites of clathrin-mediated endocytosis. *Curr. Biol.* (2011). doi:10.1016/j.cub.2011.05.048
9. Kaplan, C. *et al.* Adaptive actin organization buffers endocytosis against changes in

membrane tension. *bioRxiv* (2021).

10. Taylor, M. J., Perrais, D. & Merrifield, C. J. A high precision survey of the molecular dynamics of mammalian clathrin-mediated endocytosis. *PLoS Biol.* **9**, e1000604 (2011).
11. Kaksonen, M., Toret, C. P. & Drubin, D. G. A modular design for the clathrin- and actin-mediated endocytosis machinery. *Cell* **123**, 305–20 (2005).
12. Dambournet, D. *et al.* Genome-edited human stem cells expressing fluorescently labeled endocytic markers allow quantitative analysis of clathrin-mediated endocytosis during differentiation. *J. Cell Biol.* **217**, 3301–3311 (2018).
13. Doyon, J. B. *et al.* Rapid and efficient clathrin-mediated endocytosis revealed in genome-edited mammalian cells. *Nat. Cell Biol.* **13**, 331–7 (2011).
14. Akamatsu, M. *et al.* Principles of self-organization and load adaptation by the actin cytoskeleton during clathrin-mediated endocytosis. *Elife* (2020). doi:10.7554/eLife.49840
15. Cocucci, E., Gaudin, R. & Kirchhausen, T. Dynamin recruitment and membrane scission at the neck of a clathrin-coated pit. *Mol. Biol. Cell* **25**, 3595–3609 (2014).
16. Taylor, M. J., Lampe, M. & Merrifield, C. J. A feedback loop between dynamin and actin recruitment during clathrin-mediated endocytosis. *PLoS Biol.* **10**, (2012).
17. Grassart, A. *et al.* Actin and dynamin2 dynamics and interplay during clathrin-mediated endocytosis. *J. Cell Biol.* (2014). doi:10.1083/jcb.201403041
18. Merrifield, C. J., Feldman, M. E., Wan, L. & Almers, W. Imaging actin and dynamin recruitment during invagination of single clathrin-coated pits. *Nat. Cell Biol.* (2002). doi:10.1038/ncb837
19. María Cabeza, J., Acosta, J. & Alés, E. Dynamics and Regulation of Endocytotic Fission Pores: Role of Calcium and Dynamin. *Traffic* (2010). doi:10.1111/j.1600-

0854.2010.01120.x

20. Ramachandran, R. & Schmid, S. L. Real-time detection reveals that effectors couple dynamin's GTP-dependent conformational changes to the membrane. *EMBO J.* (2008). doi:10.1038/sj.emboj.7601961

21. Roux, A. *et al.* Membrane curvature controls dynamin polymerization. *Proc. Natl. Acad. Sci. U. S. A.* (2010). doi:10.1073/pnas.0913734107

22. Huang, B., Wang, W., Bates, M. & Zhuang, X. Three-Dimensional Super-Resolution Reconstruction Microscopy. *Science.* **319**, 810–813 (2008).

23. Xu, K., Babcock, H. P. & Zhuang, X. Dual-objective STORM reveals three-dimensional filament organization in the actin cytoskeleton. *Nat. Methods* **9**, 185–188 (2012).

24. Aguet, F., Antonescu, C. N., Mettlen, M., Schmid, S. L. & Danuser, G. Advances in analysis of low signal-to-noise images link dynamin and AP2 to the functions of an endocytic checkpoint. *Dev. Cell* (2013). doi:10.1016/j.devcel.2013.06.019

25. Boulant, S., Kural, C., Zeeh, J. C., Ubelmann, F. & Kirchhausen, T. Actin dynamics counteract membrane tension during clathrin-mediated endocytosis. *Nat. Cell Biol.* **13**, 1124–1132 (2011).

26. Li, D. *et al.* Extended-resolution structured illumination imaging of endocytic and cytoskeletal dynamics. *Science.* (2015). doi:10.1126/science.aab3500

27. Bucher, D. *et al.* Clathrin-Adaptor ratio and membrane tension regulate the flat-To-curved transition of the clathrin coat during endocytosis. *Nat. Commun.* (2018). doi:10.1038/s41467-018-03533-0

28. Saleem, M. *et al.* A balance between membrane elasticity and polymerization energy sets the shape of spherical clathrin coats. *Nat. Commun.* (2015). doi:10.1038/ncomms7249

29. Yoshida, A. *et al.* Morphological changes of plasma membrane and protein assembly during clathrin-mediated endocytosis. *PLoS Biol.* **16**, (2018).

30. Aghamohammadzadeh, S. & Ayscough, K. R. Differential requirements for actin during yeast and mammalian endocytosis. *Nat. Cell Biol.* **11**, 1039–42 (2009).

31. Kaksonen, M., Sun, Y. & Drubin, D. G. A Pathway for Association of Receptors, Adaptors, and Actin during Endocytic Internalization. *Cell* **115**, 475–87 (2003).

32. Ferguson, S. *et al.* Coordinated Actions of Actin and BAR Proteins Upstream of Dynamin at Endocytic Clathrin-Coated Pits. *Dev. Cell* **17**, 811–22 (2009).

33. Durrbach, A., Louvard, D. & Coudrier, E. Actin filaments facilitate two steps of endocytosis. *J. Cell Sci.* **109**, 457–65 (1996).

34. Lamaze, C., Fujimoto, L. M., Yin, H. L. & Schmid, S. L. The actin cytoskeleton is required for receptor-mediated endocytosis in mammalian cells. *J. Biol. Chem.* **272**, 20332–5 (1997).

35. Miya Fujimoto, L., Roth, R., Heuser, J. E. & Schmid, S. L. Actin assembly plays a variable, but not obligatory role in receptor-mediated endocytosis in mammalian cells. *Traffic* (2000). doi:10.1034/j.1600-0854.2000.010208.x

36. Lampe, M., Vassilopoulos, S. & Merrifield, C. Clathrin coated pits, plaques and adhesion. *J. Struct. Biol.* (2016). doi:10.1016/j.jsb.2016.07.009

37. Avinoam, O., Schorb, M., Beese, C. J., Briggs, J. A. G. & Kaksonen, M. Endocytic sites mature by continuous bending and remodeling of the clathrin coat. *Science.* (2015). doi:10.1126/science.aaa9555

38. Scott, B. L. *et al.* Membrane bending occurs at all stages of clathrincoat assembly and defines endocytic dynamics. *Nat. Commun.* (2018). doi:10.1038/s41467-018-02818-8

39. Sochacki, K. A. *et al.* The structure and spontaneous curvature of clathrin lattices at the plasma membrane. *bioRxiv* (2020).

40. Grimm, J. B. *et al.* A general method to fine-tune fluorophores for live-cell and in vivo imaging. *Nat. Methods* **14**, 987–994 (2017).

Acknowledgments: MJ was funded by American Heart Association Postdoctoral Fellowship (18POST34000029). DGD was funded by NIH MIRA grant R35GM118149. KX is a Chan Zuckerberg Biohub investigator and acknowledges support from NIH (DP2GM132681). SU was funded by Philomathia Foundation and the Chan Zuckerberg Initiative Imaging Scientist program. The authors would like to thank Dr. Yidi Sun and Dr. Matthew Akamatsu for insightful comments on the manuscript; the Conklin Lab at UCSF for providing WTC10 human iPSC line; the Lavis Lab at Janelia Farm for providing JF635 HaloTag ligand; Dr. Sun Hae Hong for generating the AP2-tagRFP-T iPSC cell line; the UC Berkeley QB3 MacroLab for purified S. pyogenes NLS-Cas9; the UC Berkeley Cancer Research Laboratory Flow Cytometry Facility for iPSC sorting.

METHODS

Cell culture

The WTC10 hiPSC line was obtained from the Bruce Conklin Lab at UCSF. hiPSCs were cultured on Matrigel (hESC-Qualified Matrix, Corning) in StemFlex medium (Thermo Fisher) with Penicillin/ Streptomycin in 37°C, 5% CO2. Cultures were passaged with Gentle Cell Dissociation reagent (StemCell Technologies, Cat#: 100-0485) twice every week.

Genome-editing

The AP2M1 gene was edited in WTC10 hiPSCs as previously described using TALENs targeting exon 7 of the AP2M1 gene (1). Both alleles of AP2M1 were tagged with tagRFP-T. The Cas9-crRNAtracrRNA complex electroporation method was used sequentially to edit DNM2 and ARPC3 gene in AP2M1-tagRFP-T genome-edited hiPSCs, as previously described (2, 3). The same method was used to edit the WASL gene in AP2M1-tagRFP-T/DNM2-tagGFP2 genome edited hiPSCs. *S. pyogenes* NLS-Cas9 was purified in the University of California Berkeley QB3 MacroLab. TracrRNA and crRNA that target CCTGCTCGACTAGGCCTCGA (DNM2), CCTGGACAGTGAAGGGAGCC (ARPC3) and AGCTCATGGTTTCGCCGGCG (WASL), were purchased from IDT. Gibson assembly (New England Biolabs) was used to construct donor plasmids containing DNM2 5' homology-ggtaccagtggcggaagc-tagGFP2-DNM2 3' homology, ARPC3 5' homology-ggatccggtaccagcgatccaccggtcgccacc-HaloTag-ARPC3 3' homology, and WASL 5' homology-HaloTag-agcgatccaccggtcgccaccggatcc-WASL 3' homology sequences, respectively. Three days after electroporation (Lonza, Cat#: VPH-5012) of the Cas9-crRNA-tracrRNA complex and donor plasmid, the tagGFP2 or HaloTag positive cells

were single cell sorted using a BD Bioscience Influx sorter (BD Bioscience) into Matrigel-coated 96-well plates. Clones were confirmed by PCR and Sanger sequencing of the genomic DNA locus around the insertion site. Both alleles of DNM2 and ARPC3 were tagged with tagGFP2 and HaloTag, respectively, and one allele of WASL was tagged with HaloTag in the hiPSC lines used in this study.

Western blotting

Cells were dissociated from the well using Gentle Cell Dissociation reagent (StemCell Technologies, Cat#: 100-0485). Total proteins were extracted by adding 1ml of cold 10% TCA to the cell pellets, incubated on ice for 30min, and spun down by centrifuging at 4 °C, 12000rpm for 10min. Protein pellets were dissolved in loading buffer (50 mM HEPES, pH 7.4, 150 mM NaCl, 1 mM MgCl2, 5% BME, 5mM DTT and protease inhibitor) and loaded onto an acrylamide gel for SDS-PAGE and transferred to nitrocellulose membranes for immunoblotting. Blots were incubated overnight at 4°C with primary antibodies targeting Tag(CGY)FP (1:2000 dilution in 1% milk, Evrogen, Cat#: AB121), HaloTag (1:1000 dilution in 0.5% milk, Promega, Cat#: G9211), GAPDH (1:100,000 dilution in 0.5% milk, Proteintech, Cat#: 10494-1-AP), respectively, and subsequently incubated in the dark at room temperature for 1hr with secondary antibodies.

TIRF live-cell imaging

Two days before imaging, hiPSCs were seeded onto Matrigel-coated 4-well chambered cover glasses (Cellvis). Halotag was labeled by JF635- HaloTag ligand (4). Cells were incubated in StemFlex medium with 100 mM JF635-HaloTag for 45min and the unbound ligands were

washed away by three washes with 5 min incubation in prewarmed StemFlex medium. Cells were imaged on a Nikon Ti-2 inverted microscope fitted with TIRF optics and a sCMOS camera (Hamamatsu). Cells were maintained at 37 °C with a stage top incubator (OKO Lab) in StemFlex medium with 10mM HEPES. Images were acquired with Nikon Elements. Channels were acquired sequentially at a 1 sec interval and 300ms exposure time over 4 minutes.

TIRF image processing

Four generalized processing steps were applied identify of clathrin-coated pits with single DNM2 peaks: track feature abstraction, feature dimensionality reduction, event clustering, and DNM2-peak detection. First, tracks that are defined by fitted positions and intensities for single events were generated using cmeAnalysis (5). Then, AP2 and DNM2 tracks were decomposed into dynamic features describing the dynamics of the events' position and brightness. The mapping of each track to discrete features was done to generalize the dynamics of tracked events into a set of interpretable coordinates. These features were clustered after feature scaling to normal distributions, dimensionality reduction with principal component analysis, and Gaussian mixture modeling. DNM2-positive events represented a distinct cluster of tracks that had detectable DNM2 throughout the event, were long lived, and were below the threshold of motility expected for transient, non-CME-derived clathrin-coated vesicle "visitors" at the TIRF field. Single DNM2-peak events were found by searching over a range of values set for the minimum DNM2 peak height, width, and peak-to-peak temporal distance. After finding single-peaked events in a fixed peak-parameter combination, the lifetime distribution of single peak events' lifetimes were fit to the expected underlying distribution, a Rayleigh distribution (6), where the best-fitting parameter combination was chosen to identify single-peaked events. Single

DNM2-peaked events were kept as CME sites for the remainder of the analysis. All code associated with this analysis, generating Figures 3-5, and a detailed step-by-step protocol, are available at https://github.com/DrubinBarnes/Jin_Shirazinejad_et_al_branched_actin_manuscript.

Two-color 3D STORM imaging

12 mm round coverslips were sonicated in distilled water and sterilized for 20 min in 70% ethanol, air-dried and coated with Matrigel in 24-well plates. Cells were seeded onto Matrigel-coated coverslips two days before fixation. For clathrin and actin two-color imaging, cells were fixed first for 1 min in 0.3% (v/v) glutaraldehyde (GA) solution containing 0.25% (v/v) Triton in cytoskeleton buffer (CB: 10mM MES, 150mM NaCl, 5mM EGTA, 5mM Glucose, 5mM $MgCl_2$, 0.005% NaN_3, pH 6.1) and then immediately fixed for 20 min in 2% (v/v) GA solution in CB. Both solutions were prepared fresh from a 10% GA stock (Electron Microscopy Science, cat #16120). After fixation, samples were incubated twice for 5 min in freshly prepared 0.1% (w/v) NaBH4 in PBS. For clathrin and ARPC3-HaloTag imaging, cells were fixed for 20 min in 4% (v/v) PFA (Electron Microscopy Sciences, Cat#: 15710) in CB. Subsequently, both types of samples were washed 3 times for 10 min in PBS. Samples were then blocked for 20 min in blocking buffer [3% (w/v) BSA and 0.1% (w/v) Saponin in PBS]. Clathrin light chain (Invitrogen, Cat#: MA5-11860, 1:200 dilution) and Halotag (Promega, Cat#: G9281, 1:200 dilution) antibodies were used in blocking solution. Primary antibody immunostaining was performed overnight at 4°C. On the next day, samples were washed three times in washing buffer (0.1x blocking buffer in PBS) for 10 min. Samples were incubated with secondary antibody in blocking buffer for 30 min at room temperature in the dark and were washed three

times for 10 min in washing buffer, and then three times for 10 min in PBS. Homemade mouse secondary antibody-CF680 (1:50) was used to stain clathrin and actin samples. Commercial mouse secondary antibody-AF647 (ThermoFisher, cat#A32787; 1:400) and homemade rabbit secondary antibody-CF680 (1:50) were used to stain the clathrin and ARPC3-HaloTag. Clathrin and actin samples were then stained with 0.5μM Phalloidin-AF647 (Fisher Scientific, Cat#: A22287) in PBS and kept at room temperature in the dark for 2 hours. Samples were washed three times with PBS before STORM imaging.

STORM imaging was performed as previously described on a homebuilt STORM setup (7, 8). Samples labeled by AF647 and CF680 were excited by an 647nm laser. The emission of both AF647 and CF680 was then split into two light paths as two channels using a dichroic mirror (Chroma, cat#T685lpxr), and each channel was projected onto one-half of an EMCCD camera (Andor iXon Ultra 897). Color assignment of each localization was based on its intensity in the two channels. A cylindrical lens was inserted into the transmitted channel to acquire 3D localization (9). 3D position of each localization was determined from the ellipticity of each point spread function.

References

1. Hong, S. H. *et al*. Machine-Learning-Based Analysis in Genome Edited Cells Reveals the Efficiency of Clathrin-Mediated Endocytosis. *Cell Rep*. **12**, 2121– 2130 (2015).

2. Dambournet, D. *et al.* Genome-edited human stem cells expressing fluorescently labeled endocytic markers allow quantitative analysis of clathrin-mediated endocytosis during differentiation. *J. Cell Biol*. **217**, 3301–3311 (2018).

3. Akamatsu, M. *et al.* Principles of self-organization and load adaptation by the actin cytoskeleton during clathrin-mediated endocytosis. *Elife* https://doi:10.7554/eLife.49840 (2020).

4. Grimm, J. B. *et al.* A general method to fine-tune fluorophores for live-cell and in vivo imaging. *Nat. Methods*. **14**, 987–994 (2017).

5. Aguet, F. *et al.* Advances in Analysis of Low Signal-to-Noise Images Link Dynamin and AP2 to the Functions of an Endocytic Checkpoint. *Dev. Cell* **26**, 279-291(2013).

6. Loerke, D. *et al*. Cargo and Dynamin Regulate Clathrin-Coated Pit Maturation. *PLOS Biol.* https://doi.org/10.1371/journal.pbio.1000057 (2009).

7. Kaplan, C. *et al.* Adaptive actin organization buffers endocytosis against changes in membrane tension. Preprint at https://www.biorxiv.org/content/10.1101/2020.04.05.026559v2 (2021).

8. Wojcik, M. *et al.* Graphene-enabled electron microscopy and correlated super-resolution microscopy of wet cells. *Nat Commun* **6,** 7384 (2015).

9. Huang, B. *et al.* Three-dimensional Super-resolution Imaging by Stochastic Optical Reconstruction Microscopy. *Science* **319**, 810-813 (2008).

Fig. 1: Two-color, 3D stochastic optical reconstruction microscopy (STORM) shows that actin structures are off-centered with respect to clathrin coats.

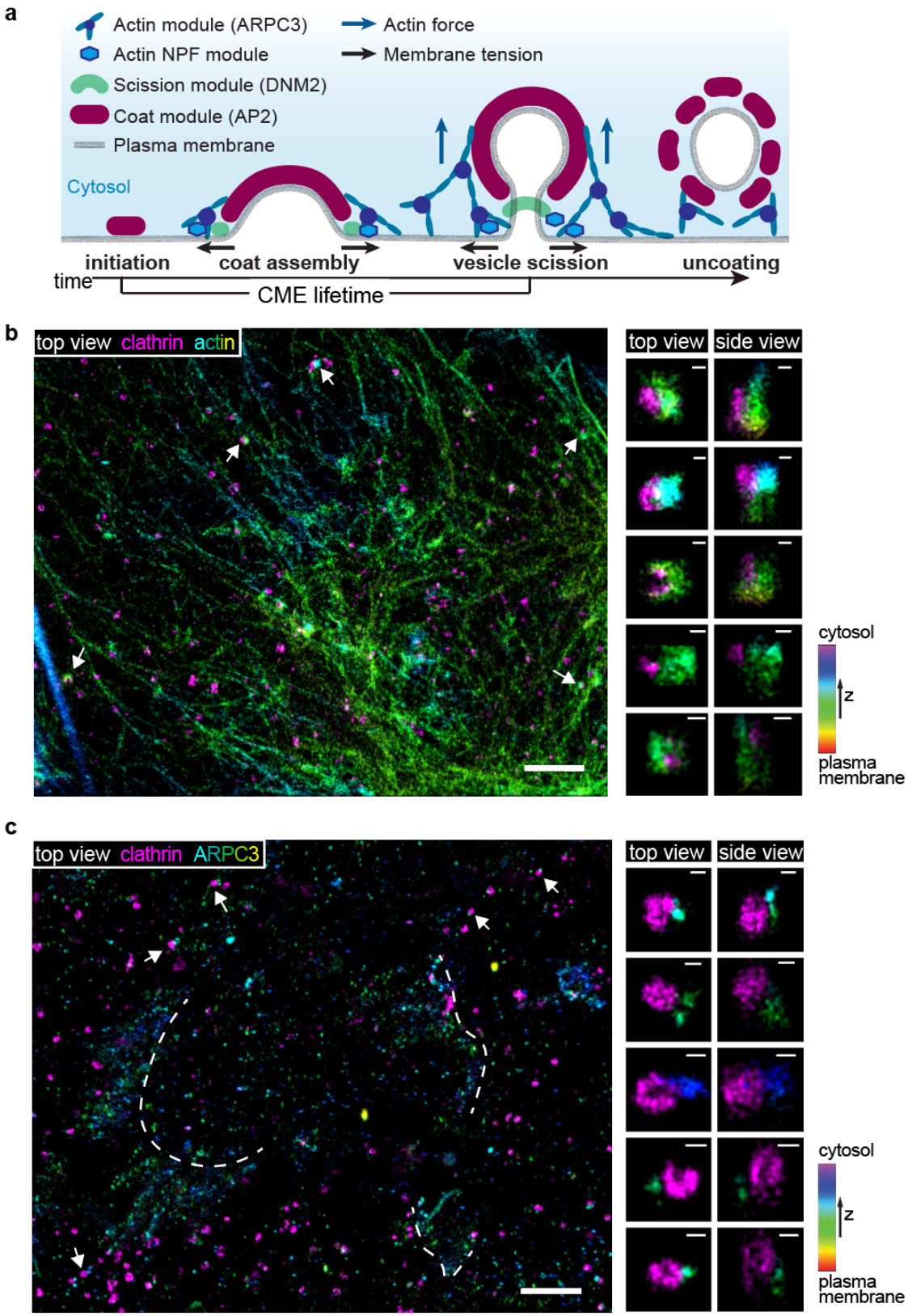

Fig. 1: Two-color, 3D stochastic optical reconstruction microscopy (STORM) shows that actin structures are off-centered with respect to clathrin coats. a, Schematic model of CME. Mammalian CME proteins can be grouped into several modules, including the coat, WASP and Myosin / actin nucleation promoting factor (NPF), actin and scission modules[5]. Actin networks provide pulling forces to invaginate the membrane against membrane tension[5,14,25]. **b,** Two-color 3D STORM image of bottom membrane of ADA cells immunolabeled with clathrin light chain antibody (clathrin, CF-680, magenta) and phalloidin (actin, AF647, rainbow). **c,** Two color 3D STORM image of the bottom membrane of ADA cells immunolabeled with clathrin light chain antibody (clathrin, AF647, magenta) and HaloTag antibody (ARPC3-HaloTag, CF-680, rainbow). Dotted lines label lamellipodia. **b, c,** The highlighted CME sites are labeled by white arrows and are rotated and shown in magnified top view and side view projections. Color bar shows the z position of ARPC3-HaloTag. Scale bars: 2μm, 100nm.

Fig. 2: Triple-genome-edited iPS cells reveal dynamic actin organization at CME sites.

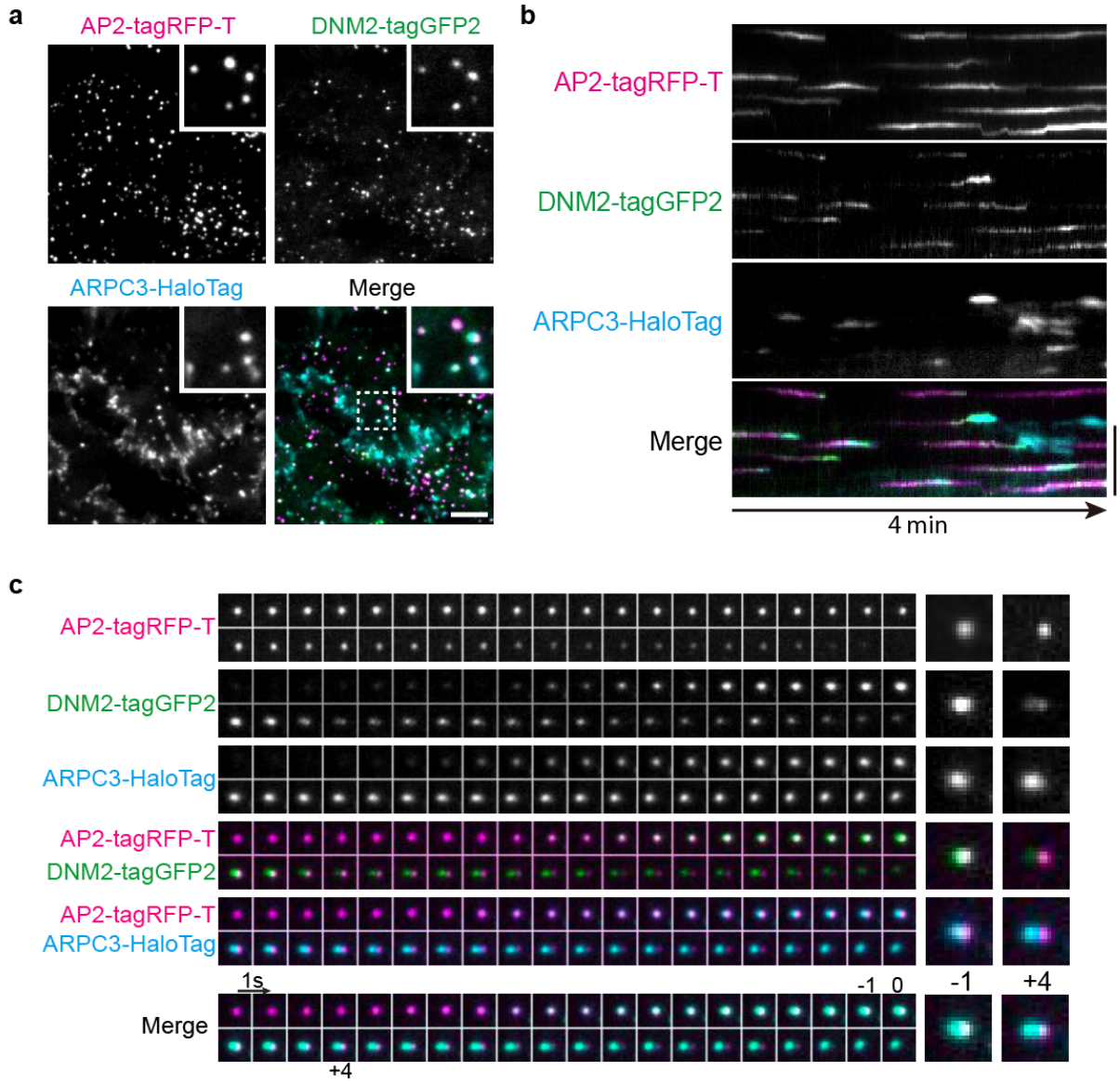

Fig. 2: Triple-genome-edited iPS cells reveal dynamic actin organization at CME sites. a, A representative single time frame image of a TIRF movie (Supplementary Video 2) of AP2M1-tagRFP-T (magenta), DNM2-tagGFP2 (green) and JF635 ligand[40]-conjugated ARPC3-HaloTag (cyan) in ADA cells. The highlighted region is boxed by a dashed line. Scale bar: 5µm. **b,** A representative kymograph of AP2M1-tagRFP-T (magenta), DNM2-tagGFP2 (green) and JF635 ligand-conjugated ARPC3-HaloTag (cyan) at CME sites in ADA cells. Scale bar: 5µm. **c,**

Montage of a representative ARPC3 positive CME site in ADA cells. Individual channels and pair-wise and triple (bottom) merges are shown. The “0” frame indicates the timing of the DNM2 peak / vesicle scission. The images of the frames 1 second before (-1) and 4 seconds after (+4) scission are highlighted. Size of field of view: 2µm x 2µm. Intervals: 1sec.

Fig. 3: Computational analysis of ARPC3 positive CME sites reveals asymmetric actin network assembly at the late stage of CME.

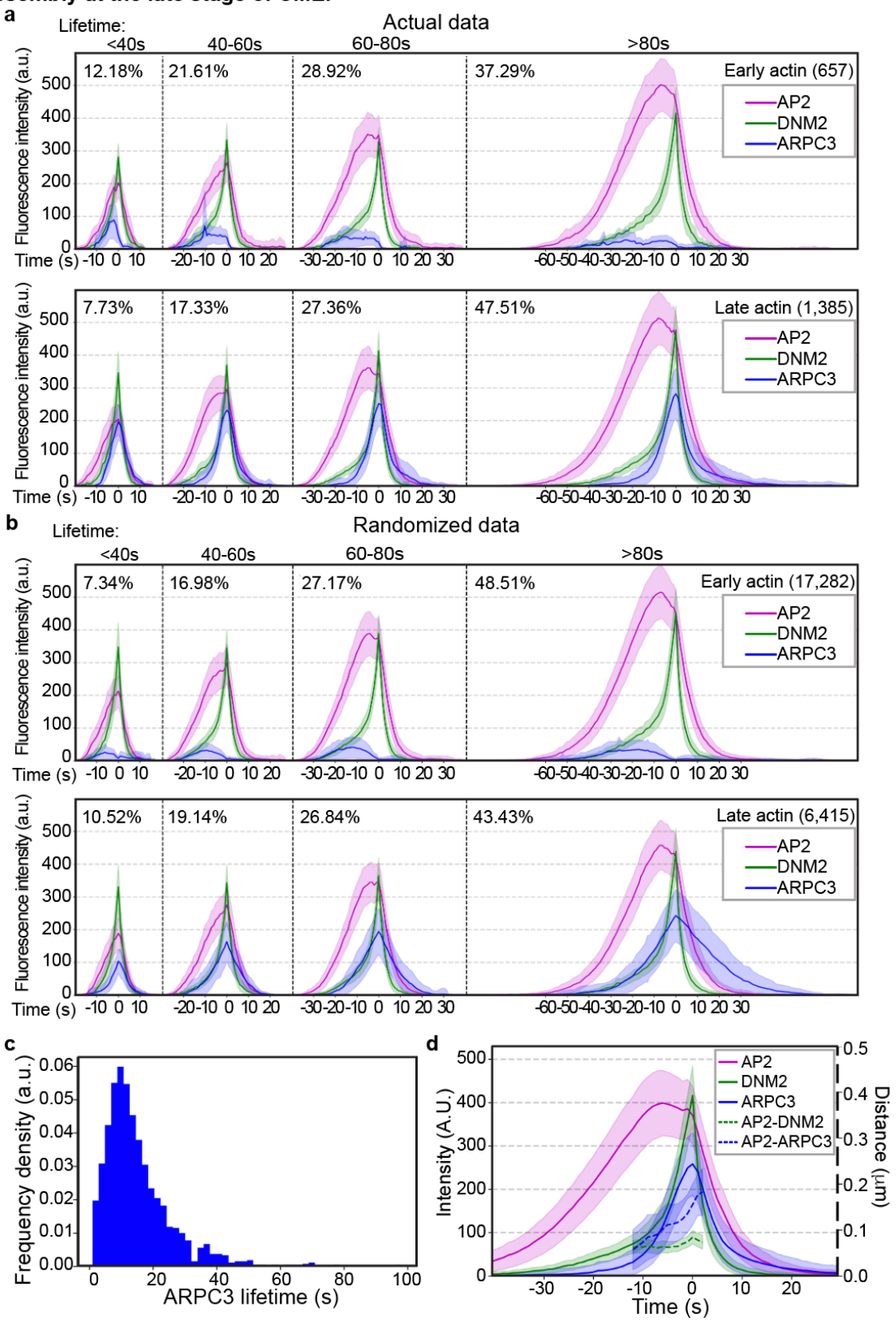

Fig. 3: Computational analysis of ARPC3 positive CME sites reveals asymmetric actin network assembly at the late stage of CME. a, b, Averaged intensity vs time plots of cohorts of ARPC3 positive CME sites in ADA cells (**a**) and in the randomized data set (**b**). Events are grouped by the timing of ARPC3-labeled branched actin network recruitment (early: top, late: bottom), and then grouped into cohorts by the lifetimes of AP2 and aligned to the frames showing the maximum DNM2 intensity (time = 0s). Total number of CME sites in each group is shown in parentheses. Percentage of the number of the CME sites in each cohort is shown next to the plot. **c,** Histogram of ARPC3-mediated actin network assembly duration. The assembly duration is measured from the first frame of the ARPC3 signal to the presumed scission time (the peak of DNM2 signal). **d,** Averaged intensity (solid lines) and distance (dashed lines) vs time plots of ARPC3 positive CME sites in ADA cells. Events are aligned to the frames showing the maximum DNM2 intensity (time = 0s). Distance between centers of two signals are shown from -10s to 3s when DNM2 and ARPC3 signals are relatively high. N=1,385. **a, b, d,** Error bar: ¼ standard deviation.

Fig. 4: Actin positive CME sites show distinct dynamics.

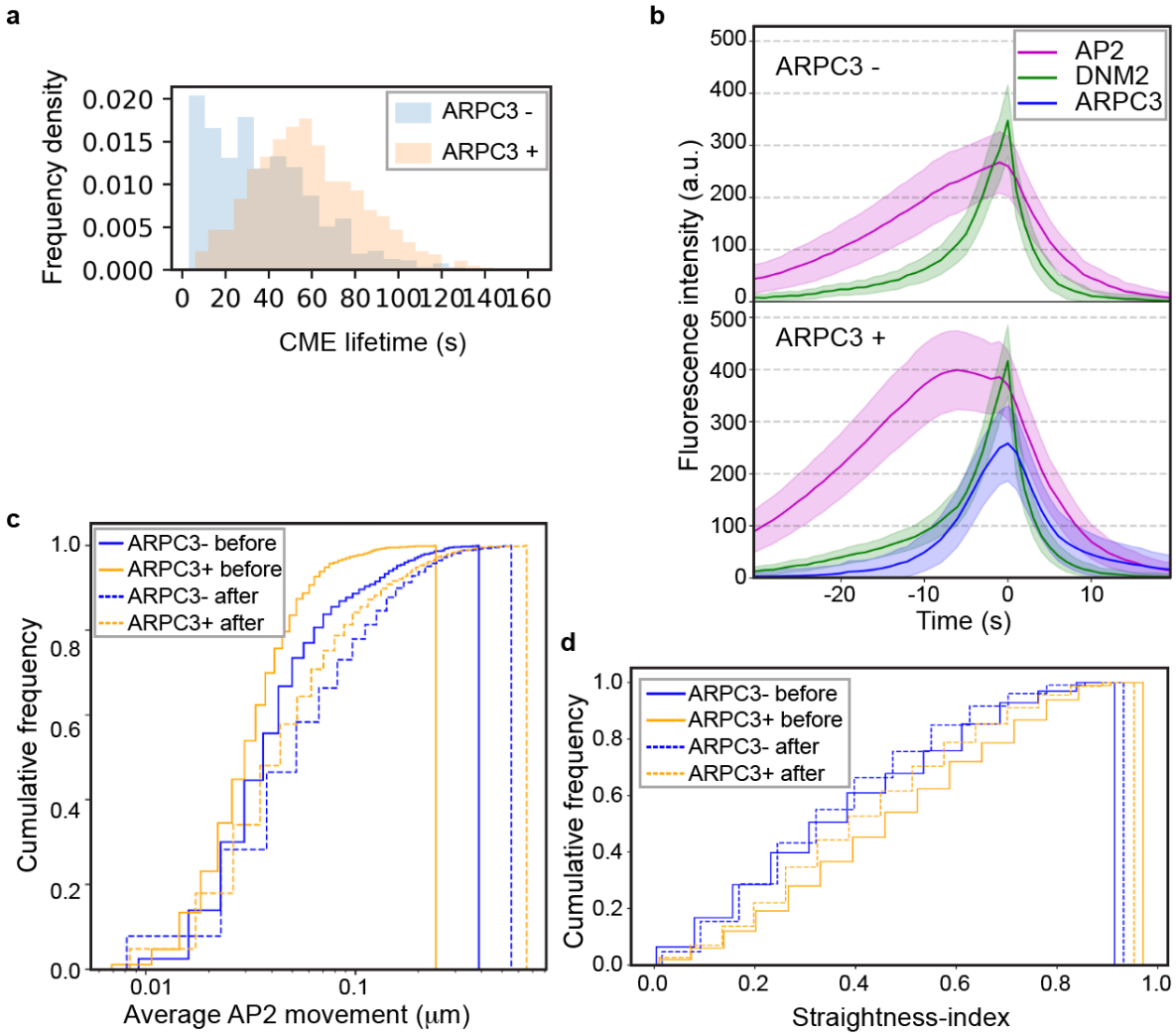

Fig. 4: Actin positive CME sites show distinct dynamics. a, Histograms of ARPC3 negative (blue) and positive (orange) CME lifetimes. CME lifetime is measured from the first frame of the AP2 signal to the presumed scission time (the peak of DNM2 signal). ARPC3 positive CME events have longer lifetimes. **b,** Averaged intensity vs time plots of ARPC3 negative (top) and positive (bottom) CME sites in ADA cells. Events were aligned to the frames showing the maximum DNM2 intensity. Error bar: ¼ standard deviation. **c,** Lateral motility of ARPC3 negative (blue) and positive (yellow) CME sites before (solid line) and after (dashed line) vesicle

scission. ARPC3 positive CME sites move slower than ARPC3 negative ones. **d,** Straightness-index of ARPC3 negative (blue) and positive (yellow) CME sites before (solid line) and after (dashed line) scission. The straightness-index is defined by the ratio between the sum of frame-to-frame distances to the end-to-end distance of a single event's trajectory, where a perfectly straight-lined trajectory would have an index of 1. APRC3 positive CME sites move with a straighter trajectory. **a-d,** ARPC3 -: N=840, ARPC3 +: N=1,385.

Fig. 5: Asymmetric N-WASP recruitment to CME sites.

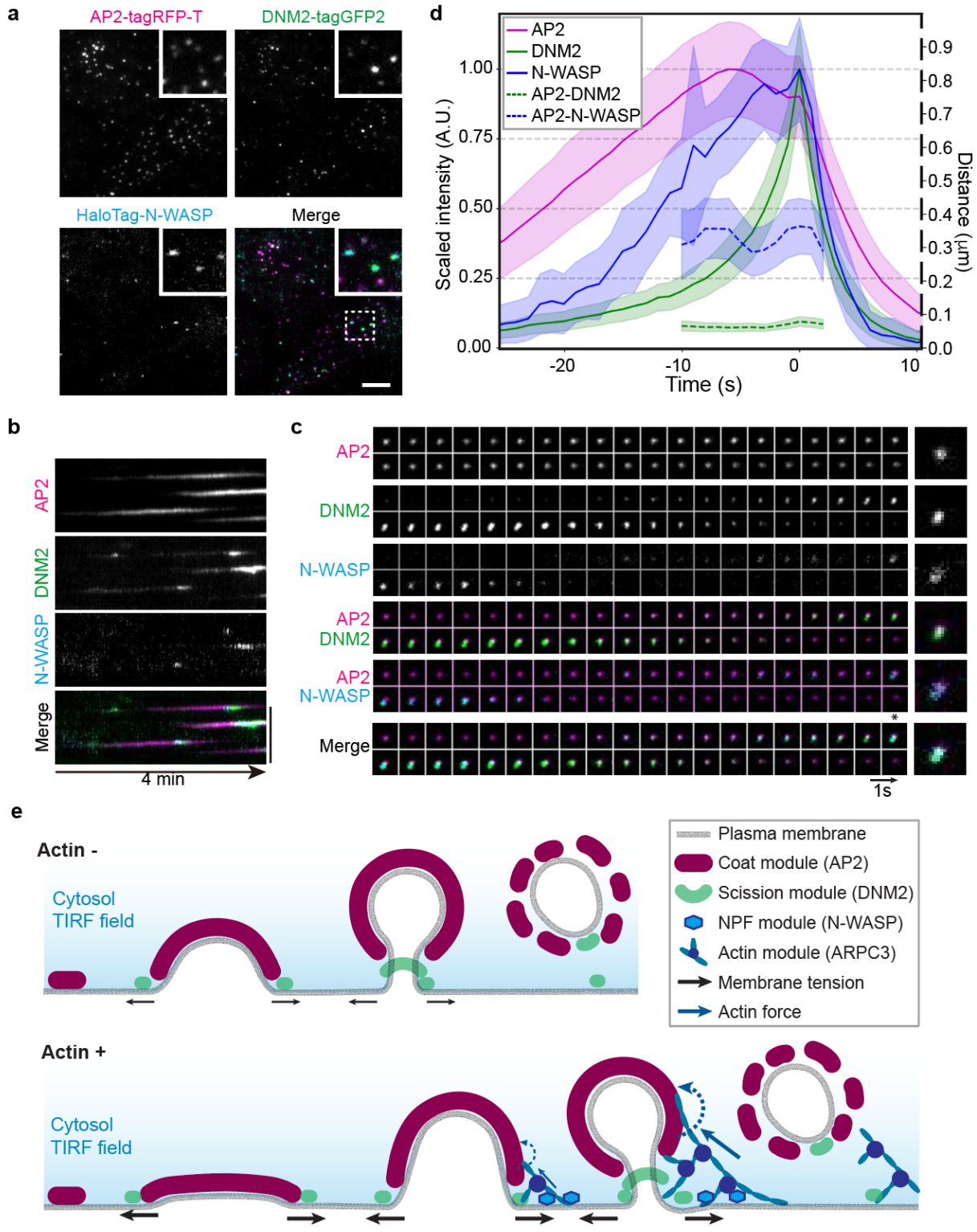

Fig. 5: Asymmetric N-WASP recruitment to CME sites. a, A representative single time frame image of a TIRF movie (Supplementary Video 4) of AP2M1-tagRFP-T (magenta), DNM2-tagGFP2 (green) and JF635 ligand-conjugated HaloTag-N-WASP (cyan) in ADW cells. The highlighted region is boxed by a dashed line. Scale bar: 5µm. **b,** A representative kymograph of CME sites in ADW cells over a 4 min movie. Scale bar: 5µm. **c,** Montages of a representative N-WASP positive CCP in ADW cells. Pair-wise and triple (bottom) merges are shown. Images from a time before the scission (*) is marked to show the displacement between the CME coat (AP2) and N-WASP. Field of the view: 2µm x 2µm. Intervals: 1s. **d,** Averaged intensity (solid line) and distance (dashed line) vs time plots of N-WASP positive CME sites in ADW cells. Events are aligned to the frames showing the maximum DNM2 intensity. Intensity is scaled to 1 at peaks for each channel. N=1,381. Error bar: ¼ standard deviation. **e,** An updated schematic model of actin negative and actin positive CCPs in human cells. Actin assembly is induced at stalled CME sites, where asymmetric forces pull, bend and possibly twist the plasma membrane against membrane tension to drive membrane invagination and vesicle scission.

Extended Data Fig 1. Genome-edited iPSCs show dynamic CME sites.

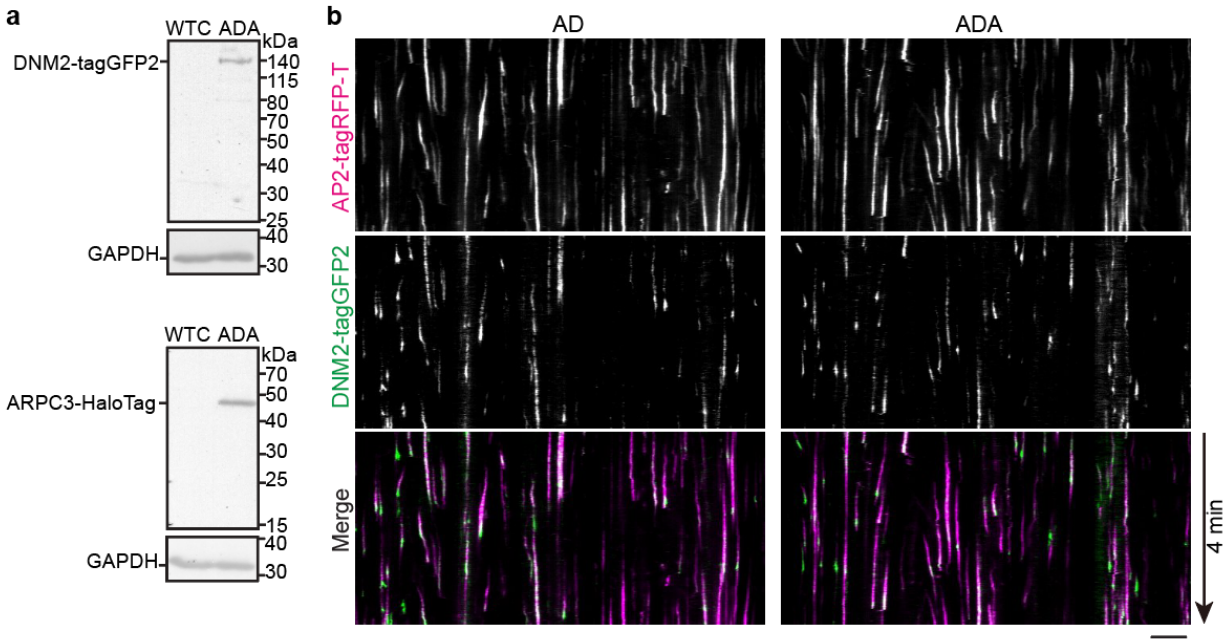

Extended Data Fig 1. Genome-edited iPSCs show dynamic CME sites. a, Immunoblot analysis of cell extracts from the WT (WTC) and genome-edited (AP2M1-tagRFP-T/DNM2-tagGFP2/ARPC3-HaloTag; ADA) human iPSCs. The labeled proteins were detected with tag(CGY)FP, HaloTag, and GAPDH (loading control) antisera respectively. **b,** Kymograph of representative CME sites of double-edited (AP2M1-tagRFP-T/DNM2-tagGFP2; AD) and triple-edited (AP2M1-tagRFP-T/DNM2-tagGFP2/ARPC3-HaloTag; ADA) cells.

Extended Data Fig 2. Two-color, 3D stochastic optical reconstruction microscopy (STORM) shows asymmetric actin structures adjacent to the clathrin coats.

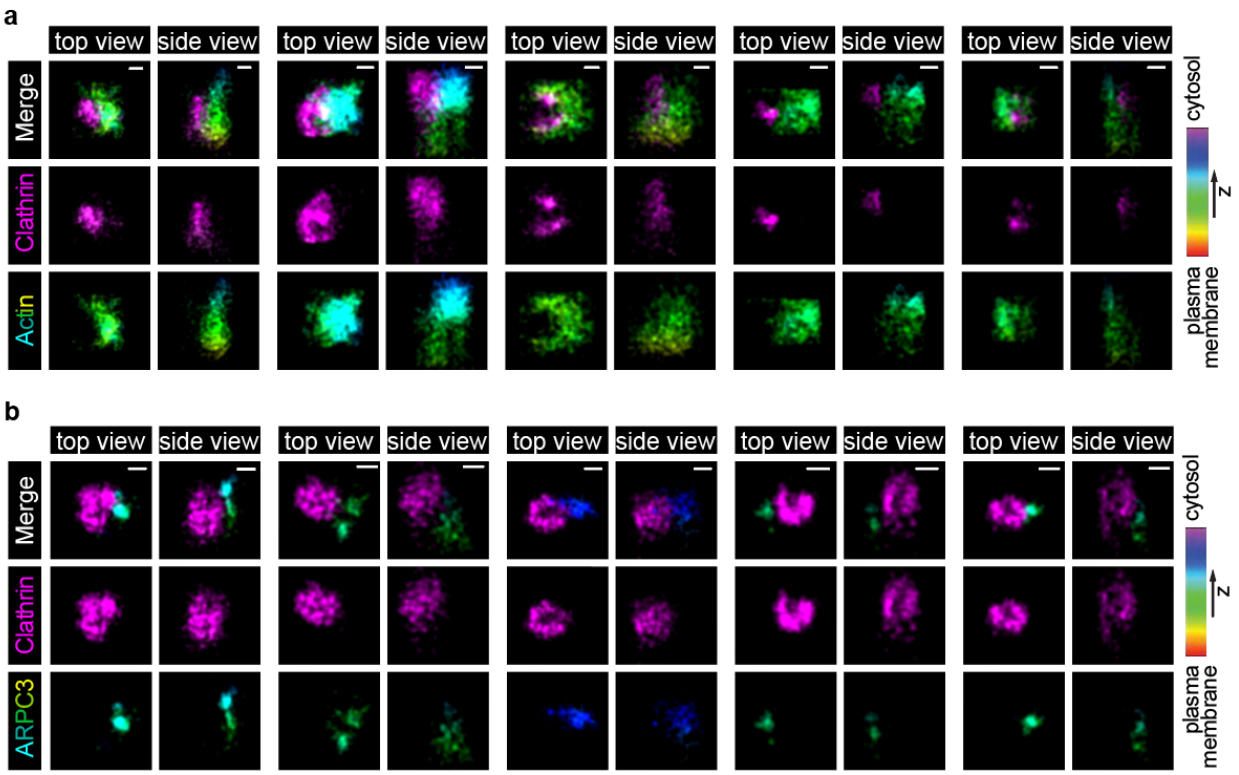

Extended Data Fig 2. Two-color, 3D stochastic optical reconstruction microscopy (STORM) shows asymmetric actin structures adjacent to the clathrin coats. a, Two-color 3D STORM of clathrin light chain (magenta) and actin (rainbow) for the highlighted CME sites from Fig. 1b. Scale bar: 100 nm. **b,** Two-color 3D STORM of clathrin light chain (magenta) and ARPC3-HaloTag (rainbow) of highlighted CME sites from Fig. 1c. Scale bars: 100 nm.

Extended Data Fig 3. Actin assembles at different types of CME sites.

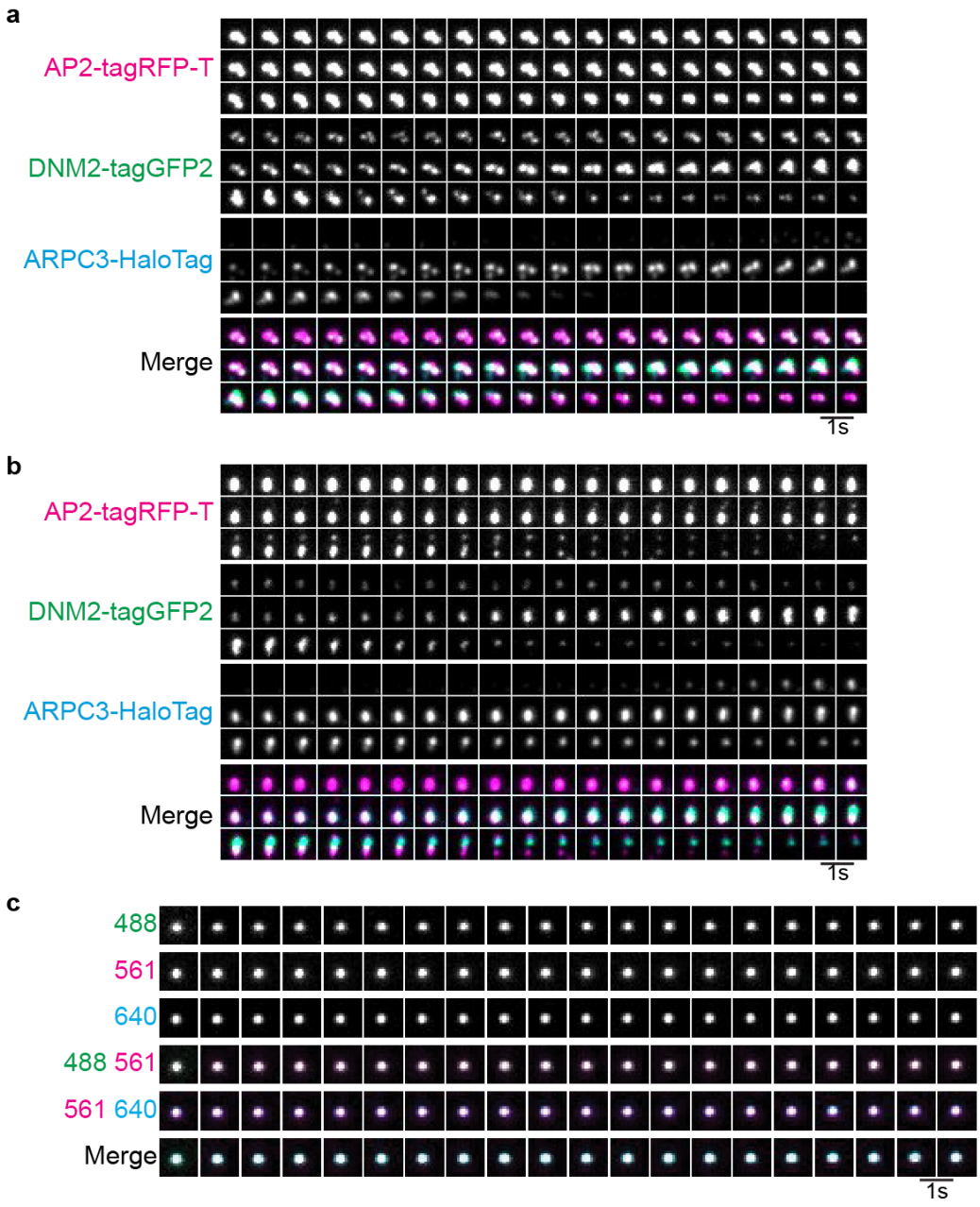

Extended Data Fig 3. Actin assembles at different types of CME sites. a, Montage of a representative ARPC3 positive CME plaque from a TIRF movie of triple-edited (AP2M1-tagRFP-T/DNM2-tagGFP2/ARPC3-HaloTag; ADA) human iPSCs (Supplementary Video 2). **b,** Montage of a representative ARPC3 positive splitting CME site from a TIRF movie of triple-

edited (AP2M1-tagRFP-T/DNM2-tagGFP2/ARPC3-HaloTag; ADA) human iPSCs (Supplementary Video 2). **c,** Montage from a TIRF movie of a multi-fluorescence bead (Supplementary Video 3). Size of field of view: 2µm x 2µm. Intervals: 1sec.

Extended Data Fig 4. Filtering methods for selection of CME sites.

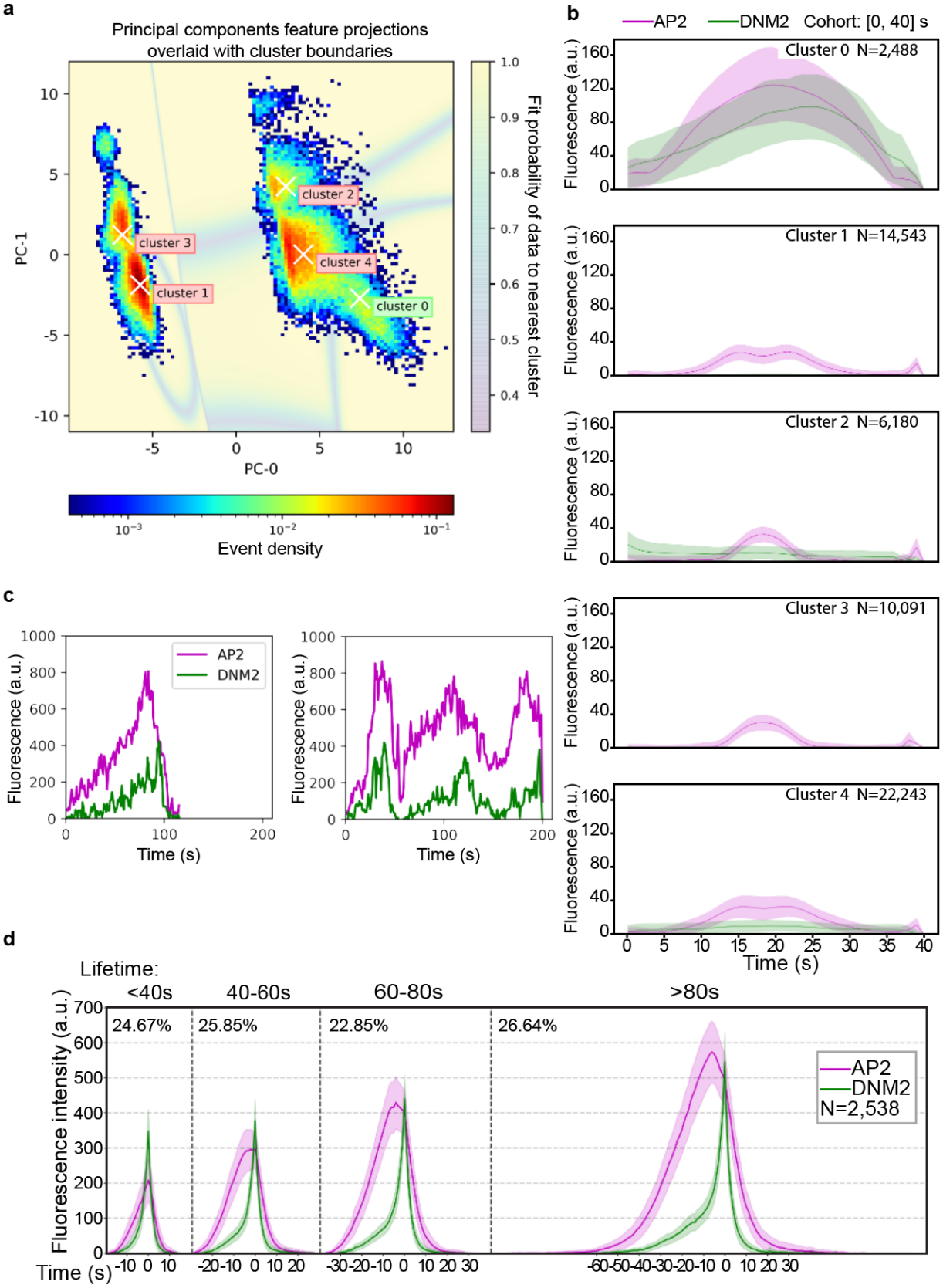

Extended Data Fig 4. Filtering methods for selection of CME sites. a, 2-D histogram of the first two principal components (PCs) of AP2 and DNM2 dynamic features. The shaded underlay represents simulated data points in principal component space and their individual probabilities of belonging to the nearest cluster center. Cluster 0 shows data points in the DNM2-positive cluster. **b,** Cohort plots of the shortest AP2 events (<40 seconds) from each cluster. Cluster 0 represents DNM2-positive events where a strong DNM2 signal is detected. **c,** DNM2-positive events are sorted by the number of DNM2 peaks using a peak-detection scheme. Representative intensity vs time plots of a single-peaked event (left) and a multi-peaked event (right). **d,** Single-peaked DNM2 events, hereon named CME sites, are grouped into lifetime cohorts and aligned to the peak of the DNM2 channel.

Extended Data Fig 5. Computational analysis reveals distinct dynamics of N-WASP positive CME sites.

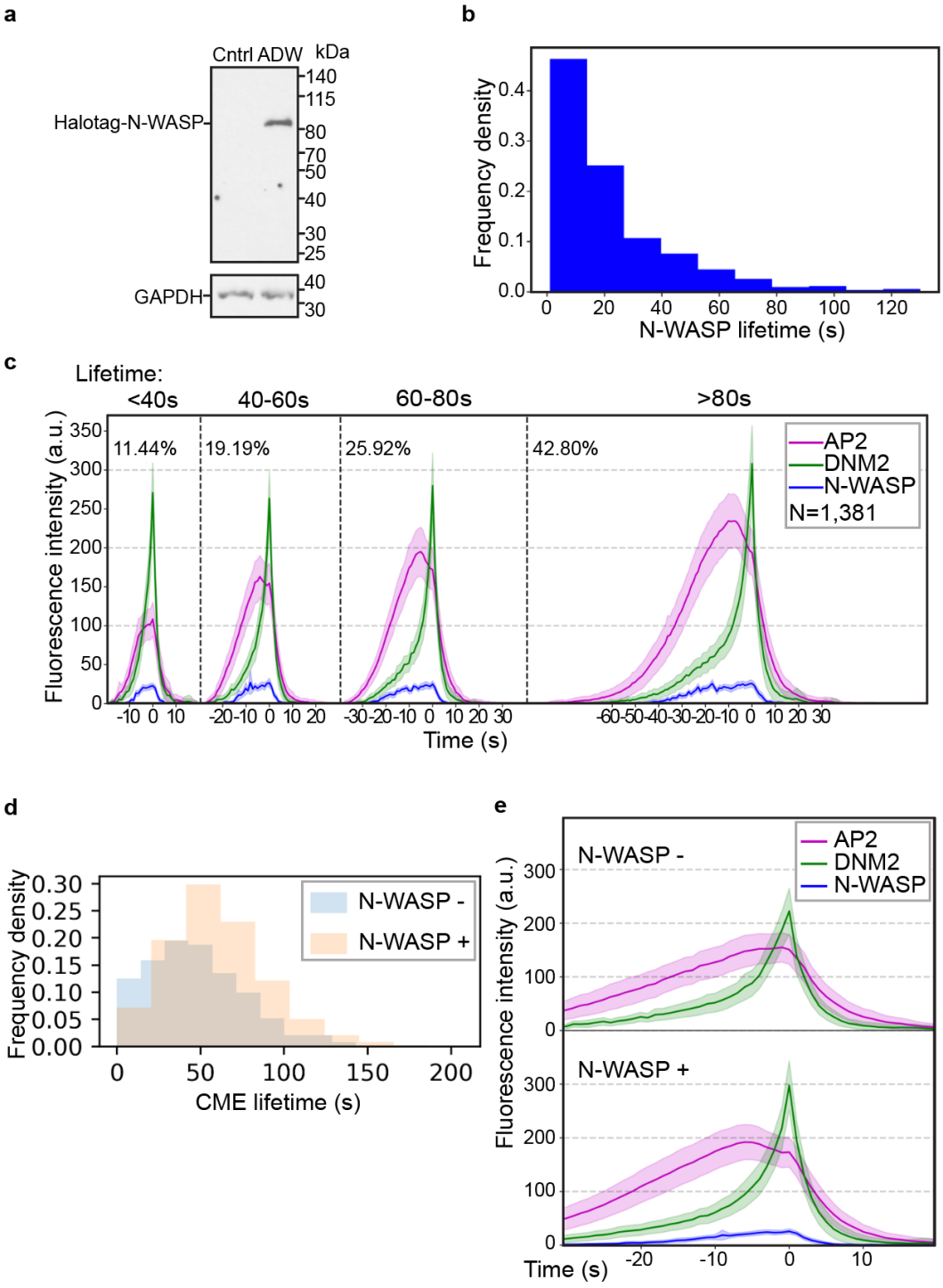

Extended Data Fig 5. Computational analysis reveals distinct dynamics of N-WASP positive CME sites. a, Immunoblot analysis of cell extracts from the control and genome-edited

(AP2M1-tagRFP-T/DNM2-tagGFP2/HaloTag-WASL; ADW) human iPSCs. The labeled proteins were detected with HaloTag and GAPDH (loading control) antisera respectively. **b,** Histogram of N-WASP lifetime at CME sites. The lifetime is measured from the first frame of the N-WASP signal to the presumed scission time (the peak of DNM2 signal). **c,** Intensity vs time plots of cohorts of N-WASP positive CME sites in ADW cells. Events are grouped into cohorts by the lifetimes of AP2 and aligned to the frames showing the maximum DNM2 intensity. **d,** N-WASP positive CME events have longer lifetimes. **e,** Intensity vs time plots of averaged N-WASP negative (top) and positive (bottom) CME sites in ADW cells. Events were aligned to the frames showing the maximum DNM2 intensity. **b-d,** N-WASP negative CME sites: N=385, N-WASP positive CME sites: N=1,381

Extended Data Fig 6. Constant curvature vs constant area models for how clathrin coats assemble at actin-positive CME sites.

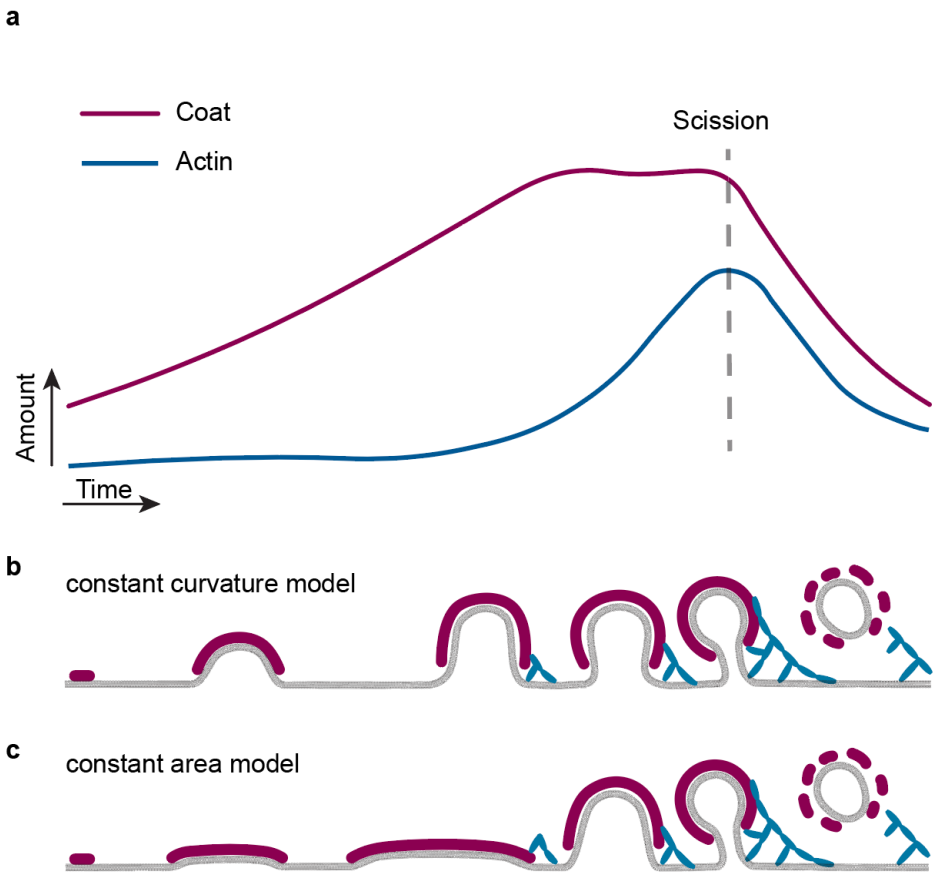

Extended Data Fig 6. Constant curvature vs constant area models for how clathrin coats assemble at actin-positive CME sites. a, A sketch showing amounts of CME coat and actin module proteins at actin-positive CME sites as a function of time based on the data in Fig. 4b. The CME coat is assembled to its maximum area around the time of actin assembly initiation. **b,** Schematic representation of constant curvature model for CME. CME coat assembles during invagination and actin assembles only at deep invaginations. **c,** Schematic representation of constant area model for CME. The CME coat expands to its maximum area first and bends during membrane invagination. In these two different scenarios, actin assembles at CME sites with different curvatures.